Journal of Applied Physics

RESEARCH ARTICLE | JANUARY 05 2024

Silicon implantation and annealing in β-Ga_2O_3: Role of ambient, temperature, and time

Katie R. Gann ; Naomi Pieczulewski ; Cameron A. Gorsak ; Karen Heinselman ; Thaddeus J. Asel ; Brenton A. Noesges ; Kathleen T. Smith ; Daniel M. Dryden ; Huili Grace Xing ; Hari P. Nair ; David A. Muller ; Michael O. Thompson

J. Appl. Phys. 135, 015302 (2024)
https://doi.org/10.1063/5.0184946

AIP Publishing

Journal of Applied Physics ARTICLE pubs.aip.org/aip/jap

Silicon implantation and annealing in β-Ga_2O_3: Role of ambient, temperature, and time

Cite as: J. Appl. Phys. **135**, 015302 (2024); doi: 10.1063/5.0184946
Submitted: 27 October 2023 · Accepted: 13 December 2023 ·
Published Online: 5 January 2024

Katie R. Gann,[1,a)] Naomi Pieczulewski,[1] Cameron A. Gorsak,[1] Karen Heinselman,[2] Thaddeus J. Asel,[3] Brenton A. Noesges,[3,4] Kathleen T. Smith,[5] Daniel M. Dryden,[6] Huili Grace Xing,[1,7,8] Hari P. Nair,[1] David A. Muller,[5,8] and Michael O. Thompson[1]

AFFILIATIONS

[1]Department of Materials Science and Engineering, Cornell University, Ithaca, New York 14853, USA
[2]National Renewable Energy Laboratory, Golden, Colorado 80401, USA
[3]Air Force Research Laboratory, Materials and Manufacturing Directorate, Wright-Patterson AFB, Ohio 45433, USA
[4]Azimuth Corporation, Beavercreek, Ohio 45324, USA
[5]School of Applied and Engineering Physics, Cornell University, Ithaca, New York 14853, USA
[6]Air Force Research Laboratory, Sensors Directorate, Wright-Patterson AFB, Ohio 45433, USA
[7]School of Electrical and Computer Engineering, Cornell University, Ithaca, New York 14853, USA
[8]Kavli Institute at Cornell for Nanoscale Science, Cornell University, Ithaca, New York 14853, USA

[a)]**Author to whom correspondence should be addressed:** krg66@cornell.edu

ABSTRACT

Optimizing thermal anneals of Si-implanted β-Ga_2O_3 is critical for low resistance contacts and selective area doping. We report the impact of annealing ambient, temperature, and time on the activation of room temperature ion-implanted Si in β-Ga_2O_3 at concentrations from 5×10^{18} to 1×10^{20} cm^{-3}, demonstrating full activation (>80% activation, mobilities >70 $cm^2/V\,s$) with contact resistances below 0.29 Ω mm. Homoepitaxial β-Ga_2O_3 films, grown by plasma-assisted molecular beam epitaxy on Fe-doped (010) substrates, were implanted at multiple energies to yield 100 nm box profiles of 5×10^{18}, 5×10^{19}, and 1×10^{20} cm^{-3}. Anneals were performed in an ultra-high vacuum-compatible quartz furnace at 1 bar with well-controlled gas compositions. To maintain β-Ga_2O_3 stability, p_{O2} must be greater than 10^{-9} bar. Anneals up to $p_{O2} = 1$ bar achieve full activation at 5×10^{18} cm^{-3}, while 5×10^{19} cm^{-3} must be annealed with $p_{O2} \leq 10^{-4}$ bar, and 1×10^{20} cm^{-3} requires $p_{O2} < 10^{-6}$ bar. Water vapor prevents activation and must be maintained below 10^{-8} bar. Activation is achieved for anneal temperatures as low as 850 °C with mobility increasing with anneal temperatures up to 1050 °C, though Si diffusion has been reported above 950 °C. At 950 °C, activation is maximized between 5 and 20 min with longer times resulting in decreased carrier activation (over-annealing). This over-annealing is significant for concentrations above 5×10^{19} cm^{-3} and occurs rapidly at 1×10^{20} cm^{-3}. Rutherford backscattering spectrometry (channeling) suggests that damage recovery is seeded from remnant aligned β-Ga_2O_3 that remains after implantation; this conclusion is also supported by scanning transmission electron microscopy showing retention of the β-phase with inclusions that resemble the γ-phase.

I. INTRODUCTION

Beta-phase gallium oxide (β-Ga_2O_3) has received attention in recent years due to its ultrawide bandgap (~4.8 eV), estimated high breakdown strength (~8 MV/cm), and optical transparency.[1,2] While other metastable polymorphs are also of interest,[3,4] the monoclinic β-phase has been extensively studied and the availability of large area melt-grown substrates is a distinct advantage over other wide and ultra-wide bandgap semiconductors.[1,5–7] β-Ga_2O_3 can be readily doped with a variety of n-type donors including Si, Ge, and Sn, with Si emerging as the dopant of choice.[8,9] *In situ* doping during epitaxial growth has been demonstrated during metalorganic chemical vapor deposition (MOCVD), pulsed laser deposition (PLD), and molecular beam epitaxy (MBE) with Si concentrations up to 2×10^{20} cm^{-3}.[10–14] Si n-type doping by ion

implantation has also been demonstrated, providing a controllable method for selective area doping in lateral devices.[15–20]

Ion implantation requires thermal annealing to remove implantation-induced lattice damage, including point and extended defects as well as radiation-induced phase transformations,[21–24] and to activate implanted dopants. Processing parameters for annealing include time, temperature, heating and cooling rates, ambient conditions, and the presence of a protective layer during annealing. Ion implantation of Si, Ge, and Sn[15,16,19] has been reported for n-type doping for channel and contact regions in β-Ga_2O_3, while implants of Mg and N have been investigated as deep acceptors for blocking layers.[16,25,26] Sasaki, in 2013, reported activation of Si after annealing between 900 and 1100 °C. While increasing temperature improved activation, significant Si diffusion was observed at 1100 °C. Sasaki also reported a decrease in activation fraction as the implanted concentration increased from 1×10^{19} to 1×10^{20} cm^{-3} Si.[15] Tadjer, in 2019, studied the lattice recovery after Si and Sn implant at doses of 2×10^{15} cm^{-2}, corresponding to peak concentrations of 2×10^{20} cm^{-3}. They reported that lattice recovery required anneals at 1150 °C for the highest dose Si implants, with higher temperatures required for Sn implants, consistent with the higher atomic mass implant generating more lattice damage.[27] In 2022, Spencer demonstrated activation of Si, Ge, and Sn implants after annealing at 925 °C for 30 min by rapid thermal annealing (RTA), achieving up to 65% activation for the implanted Si, corresponding to 1.3×10^{19} cm^{-3} and a mobility of 93 $cm^2/V\,s$.[19] Furthermore, by increasing the temperature to 600 °C during implantation, as compared to room temperature, Sardar demonstrated in 2022 an activation fraction of 82% for Si implanted to a peak concentration of 1.2×10^{20} cm^{-3}.[17]

Annealing under N_2 ambients has been shown to be favorable compared to O_2 ambients, with N_2 anneals activating carriers, while O_2 reversibly deactivates carriers and enhances Si diffusion.[28,29] Annealing in argon has been reported as similar to annealing in N_2, suggesting that the inert gas does not impact activation.[30,31] Existing literature does not quantify gas purity, especially trace concentrations of oxygen and water in N_2 or Ar ambients. Some p_{O2} is critical for annealing as β-Ga_2O_3 is unstable at high temperatures in the absence of oxygen, decomposing to the volatile Ga_2O sub-oxide or to Ga metal; above 1150 °C, β-Ga_2O_3 has been shown to decompose under nominally pure N_2 and the addition of H_2 lowered the decomposition threshold to 350 °C.[32] Lany estimated the equilibrium partial pressure of Ga_2O as a function of temperature and p_{O2},[8] indicating that limiting p_{Ga2O} to $<10^{-5}$ bar requires that the concentration of O_2 must be maintained above 10^{-14} bar at 900 °C, 10^{-10} bar at 1000 °C, and 10^{-7} bar at 1100 °C. Their DFT calculations[8] also suggested strong p_{O2} dependence for Si activation, especially at high carrier concentrations.

Despite the early successes of Si ion implantation in β-Ga_2O_3, detailed studies on the effects of annealing ambient, temperature, and time are absent from the literature. In this work, we report on the activation fraction and mobility following furnace annealing of room temperature Si implants (from 5×10^{18} to 1×10^{20} cm^{-3}) as a function of annealing ambient (controlled p_{O2} and p_{H2O}), temperature (850–1050 °C), and time (2.5–120 min). Under optimized annealing conditions, activation to >80% with mobilities >70 $cm^2/V\,s$ was observed for concentrations up to 1×10^{20} cm^{-3}.

II. EXPERIMENTAL

β-Ga_2O_3 films were grown using a Veeco GEN Xcel plasma-assisted MBE (PAMBE) system equipped with a standard effusion cell for Ga and a UNI-Bulb RF plasma source angled at 45° relative to the substrate for oxygen. Tamura Novel Crystal Technology (NCT) Fe-doped β-Ga_2O_3 (010) substrates (23 × 25 mm) were solvent cleaned prior to loading into the growth chamber, with an additional *in situ* oxygen plasma clean prior to growth. Unintentionally doped (UID) films were grown at a substrate temperature of 650 °C with a Ga beam equivalent pressure (BEP) of 6.0×10^{-8} Torr (calibrated to be near the stoichiometric conditions for the chamber), and an oxygen plasma from 2.0 SCCM of O_2 flow and 250 W of RF power. A target film thickness of 400 nm served as a buffer layer to minimize Fe diffusion from the substrate into the surface implanted layer.[33]

To compare with implanted samples, an *in situ* doped sample was grown in an Agnitron Agilis 100 MOCVD system on equivalent substrates. A ~50 nm UID layer was first grown at a reactor pressure of 15 Torr and a substrate temperature of 600 °C, followed by the growth of a ~95 nm film doped with Si at 6.9×10^{19} cm^{-3} grown at a pressure of 40 Torr and a substrate temperature of 705 °C. The substrate temperature was measured using a pyrometer aligned to the backside of the SiC-coated graphite susceptor. Triethylgallium (TEGa) and silane (25 ppm SiH_4 in argon) were used as precursors for gallium and silicon, respectively, with argon as the carrier gas and molecular oxygen as the oxidant. The TEGa molar flow was 19 and 39 μmol/min for the UID and doped layer, respectively. For the doped layer, the silane flow was 27 nmol/min. For the entire growth, the oxygen flow was set at 500 SCCM with a total gas flow of 6000 SCCM.

Prior to ion implantation, films were capped with approximately 20 nm SiO_2 via atomic layer deposition (ALD) in an Oxford FlexAL system at 300 °C using tris(dimethylamino)silane. Ion implantation was performed using three implant energies to form a 100 nm box-shaped concentration profile with straggle to ~200 nm (Fig. 1). Three Si box concentrations of 5×10^{18}, 5×10^{19}, and 1×10^{20} cm^{-3} were formed, all using similar implant energies (modified to compensate for slight variations in the ALD thickness). The nominal energies and doses for the 5×10^{19} cm^{-3} box implant were 15, 45, and 115 keV at 5.6×10^{13}, 1.4×10^{14}, 5.2×10^{14} cm^{-2}, respectively; specific implant energies for each growth were adjusted based on the measured thickness of the SiO_2 capping layer and are detailed in Table SI in the supplementary material. Figure 1 shows the simulated profile from stopping range of ions in matter (SRIM).[34] Secondary ion mass spectrometry (SIMS) measurements (Fig. S1 in the supplementary material) confirm the initial box profile and show slight diffusion after annealing at 1000 °C for 20 min.

After implant, samples were diced into 5 × 5 mm die for anneals. The SiO_2 layer was removed using a 6:1 buffered oxide etchant for 1 min. To account for small differences in UID growth and substrate quality, all trends reported for different activation conditions only include samples from one growth. While rapid thermal annealing (RTA) is often used to activate implants, furnace annealing was chosen to permit careful control of gas purity, furnace cleanliness, purging times, and temperature accuracy.

Annealing was performed in an ultra-high vacuum (UHV) compatible quartz tube furnace, shown schematically in Fig. S2 in

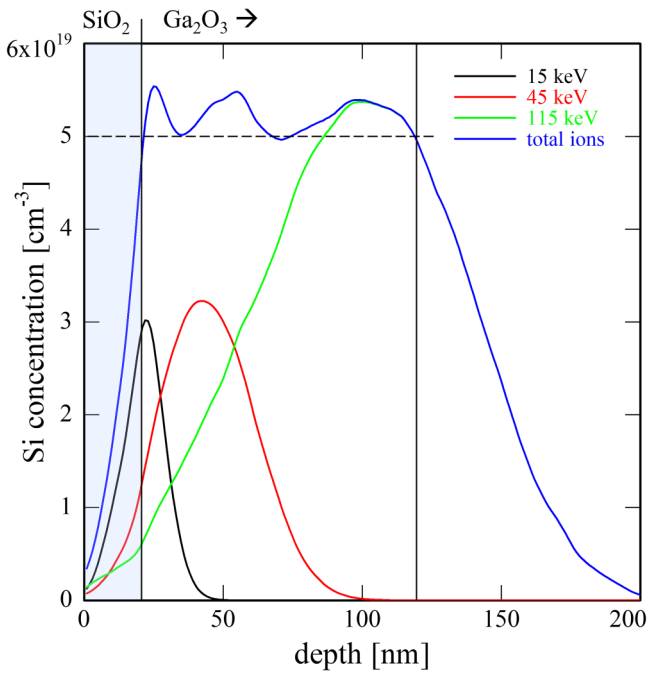

FIG. 1. Simulated implant profile of the 5×10^{19} cm^{-3} implant with 15, 45, and 115 keV at doses of 5.6×10^{13}, 1.4×10^{14}, 5.2×10^{14} cm^{-2}, respectively, creating a box-shaped implant for the first 100 nm of the film with straggle to 200 nm.

the supplementary material. Gas flows were carefully controlled through flow meters and, to minimize water vapor, the mixed gases were passed over a desiccant to reduce p_{H2O} to below 10^{-8} bar. For annealing experiments in controlled p_{H2O}, nitrogen with 10^{-4} bar H_2O was mixed into the gas stream at the inlet of the furnace. Gas from the furnace was passed through a glycerin bubbler and vented to atmosphere ensuring no backflow into the furnace. Unless otherwise specified, all samples were annealed under a 1 bar total pressure (P_{total}). When not in use, the furnace was continuously purged with 1000 SCCM of liquid nitrogen boiloff. All high purity gases were acquired from AirGas and are summarized in Table I. Gas mixtures (1% O_2 in N_2 and 100 ppm H_2O in N_2) do not specify N_2 purity. A vacuum port, open only during sample loading, minimized furnace contamination from ambient air. After loading into the furnace, a minimum 20-min gas purge with the intended high purity ambient was performed prior to moving the sample into the preheated hot zone. A discussion of the importance of purging times is included in the supplementary material. Unless otherwise stated as a second, subsequent, or staged anneal experiment, all results are for anneals of as-implanted samples.

Electrical activation was determined using a Nanometrics HL5500 Hall system with indium contacts made to the corners in a van der Pauw geometry. The active carrier fraction was defined as the ratio of the measured sheet concentration (n_s) to the total implant dose (Si/cm^2). Free carrier concentrations within the box implant were then estimated by multiplying the active carrier fraction by the total target implant concentration (Si/cm^3). On select samples, contact resistances to the highly doped films were extracted using the transfer length method (TLM). A BCl_3/Ar ICP-RIE dry etch (20 W RF and 250 W ICP) with a Ti/Ni hard mask was used for mesa isolation. The Ti/Ni hard mask was stripped using a 1:1 HF:HNO_3 solution. A Ti/Al/Ni (50/100/65 nm) stack for metal contacts was deposited by electron-beam evaporation at a base pressure of 4.5×10^{-7} Torr and was patterned via optical lithography and liftoff. TLM samples were annealed in a series of 5 s RTA cycles in N_2 from 300 to 480 °C in steps of 30 °C to ensure ohmic contact formation between the metal and the highly doped films.

X-ray diffraction (XRD) was performed using a PANalytical Empyrean diffractometer with Cu $K_{\alpha 1}$ radiation. Rutherford backscattering spectrometry in a channeling mode (RBS/c) was performed with a Model 3S-MR10 accelerator from National Electrostatics Corporation (NEC) calibrated using indium zinc oxide (IZO) on glassy carbon. Data were collected for each as-implanted and annealed sample in a 168° backscattering geometry with 2 MeV He^+ beam energy, and 40 μC per scan with one scan each in random and channeling configurations. Cross-sectional scanning transmission electron microscopy (STEM) samples were prepared using a Thermo Fisher Helios G4 UX Focused Ion Beam with a final milling step of 5 keV. A carbon layer was deposited to reduce charging during sample preparation. STEM imaging was performed with an aberration corrected Thermo Fisher Spectra 300 CFEG operated at 300 keV.

III. RESULTS AND DISCUSSION

A. Electrical activation

Previous annealing studies using N_2 ambients did not quantify p_{O2} levels and, as noted earlier, some p_{O2} is necessary to stabilize

TABLE I. High purity gas specifications from AirGas. All impurity levels are given in ppm. The terms R, RP, and UHP are used in the text to designate the specific gases in this table. N/A, not applicable for specified gas; --, not specified; *, CO + $CO_2 \leq 1$ ppm.

Product name	Minimum purity	O_2	H_2O	THC	CO	CO_2	H_2 (for N_2)	N_2 (for Ar)
Research Plus (RP) N_2	99.9999%	≤0.2	≤0.2	≤0.1	≤0.3	≤0.1	--	N/A
Research (R) N_2	99.9997%	≤0.5	≤0.5	≤0.2	≤0.5	≤0.5	≤2	N/A
Ultra-High Purity (UHP) N_2	99.999%	≤1	≤1	≤0.5	*≤ 1	*≤ 1	--	N/A
RP Ar	99.9999%	≤0.1	≤0.2	≤0.1	≤0.1	≤0.1	N/A	≤2
100 ppm H_2O in N_2	N/A	N/A	100	N/A	N/A	N/A	N/A	N/A
1% O_2 in N_2	N/A	10 000	N/A	N/A	N/A	N/A	N/A	N/A

Ga_2O_3 against decomposition. To study the p_{O2} dependence of electrical activation, samples implanted to each of the three Si concentrations were annealed under varying p_{O2} using either UHP O_2 or 1% O_2 in N_2 gas mixed with RP N_2 ($P_{total} = 1$ bar, $p_{H2O} < 10^{-8}$ bar for all conditions). After sample loading, the furnace was purged for 20 min with 2000 SCCM and samples were annealed for 10 min at 950 °C. For the lowest p_{O2} ($< 2 \times 10^{-7}$ bar, RP N_2), measured sheet resistances (R_s) were 1260, 161, and 199 Ω/□ for 5×10^{18}, 5×10^{19}, and 1×10^{20} cm^{-3} samples, respectively. R_s for the 1×10^{20} cm^{-3} sample was higher than for the 5×10^{19} sample as 10 min at 950 °C is beyond the optimal time for 1×10^{20} cm^{-3} implants, as discussed later. Figure 2 shows the relative activation as a function of p_{O2}, with the relative sheet resistance ($R_{s,rel}$) defined as R_s divided by R_s at $p_{O2} < 2 \times 10^{-7}$ bar ($R_{s,low\ pO2}$); shaded regions correspond to $R_{s,rel} > 2$. For 5×10^{18} cm^{-3}, implants activated for anneals over the full range of $2 \times 10^{-7} < p_{O2} < 1$ bar with no significant change in R_s, mobility, or activation fraction. For 5×10^{19} cm^{-3} implants, activation was insensitive to p_{O2} up to 10^{-4} bar, but at 10^{-3} bar, R_s increased by several orders of magnitude. At 1×10^{20} cm^{-3}, carriers activated only under RP N_2, $p_{O2} < 2 \times 10^{-7}$ bar; any additional O_2 caused R_s to increase dramatically (an order of magnitude at 10^{-5} bar p_{O2}). The decreased tolerance to oxygen at high doping concentrations is likely due to the increased p_{O2} and Fermi level causing an increase in V_{Ga} concentrations.[8]

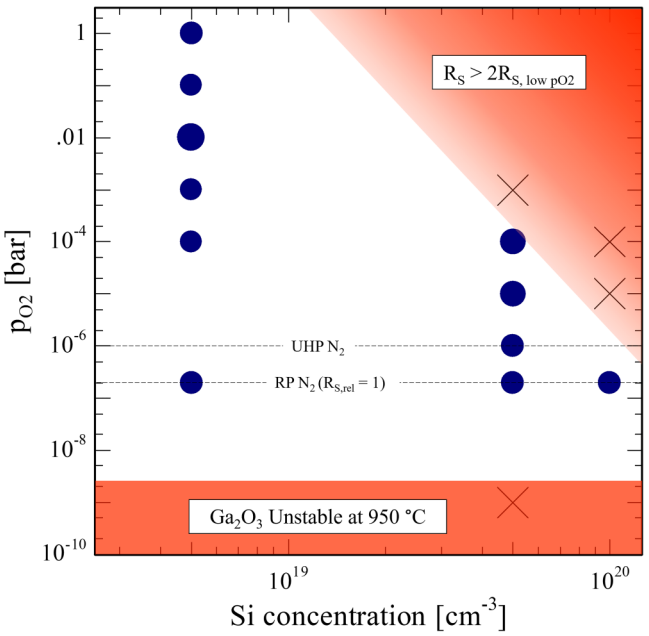

FIG. 2. p_{O2} dependence of Si activation at 950 °C for 10 min as a function of implant concentration. Experimental conditions for R_s values below $2R_{s,low\ pO2}$ ($p_{O2} < 2 \times 10^{-7}$ bar) are shown as filled circles with the diameter of the circle representing the $R_{s,rel}$ value (with $R_{s,low\ pO2} =$ "1"); black "×" symbols indicate conditions that do not result in high activation ($R_{s,rel} > 2$). Regions shaded in red are guides to the eye and represent p_{O2} values with $R_{s,rel} > 2$.

Activation behavior was equivalent during anneals in argon ($p_{O2} < 2 \times 10^{-7}$ bar), confirming that N_2 is not critical. The lower bound on p_{O2}, set by β-Ga_2O_3 stability, was evident in anneals under UHV ($P_{total} < 2 \times 10^{-9}$ bar and $p_{O2} < 10^{-9}$ bar) and forming gas (4% H_2 in N_2, $p_{O2} < 10^{-12}$ bar). UHV anneals of 5×10^{19} cm^{-3} resulted in R_s of 1–2 kΩ/□ (tenfold increase, indicated as black "×" in Fig. 2), and anneals under forming gas decomposed Ga_2O_3 (Fig. S3 in the supplementary material). Under UHV, it is unlikely that the effect is a result of the change in the total pressure but rather a result of the decreased p_{O2}. This establishes a lower bound for annealing at 950 °C of $p_{O2} > 10^{-9}$ bar. While lower Si concentration implants tolerate p_{O2} up to 1 bar, there does not appear to be any advantage to higher p_{O2} for activation.

While activation was achieved over a wide range of p_{O2}, anneals were much more sensitive to trace p_{H2O} contamination. As-implanted samples at 5×10^{19} cm^{-3} were annealed for 20 min at 950 °C under R N_2 ($P_{total} = 1$ bar, $p_{H2O} < 1 \times 10^{-8}$ bar, $p_{O2} < 5 \times 10^{-7}$ bar) mixed with controlled amounts of H_2O; p_{H2O} values of $< 1 \times 10^{-8}$, 2.5×10^{-7}, 2.5×10^{-6}, and 2.5×10^{-5} bar were tested. Figure 3 shows R_s, mobility, and activation fraction as a function of p_{H2O} after the initial anneal (blue). Even at 2.5×10^{-7} bar p_{H2O} (0.25 ppm), the activation fraction decreased. By 2.5×10^{-5} bar p_{H2O}, R_s increased by an order of magnitude as n_s decreased tenfold. Figure 3 indicates that mobility decreased only slightly with the initial H_2O addition but then increased at high p_{H2O} (likely due to reduced scattering with the lower n_s). Presence of H_2O became more detrimental with the addition of O_2 to the ambient, as discussed in the supplementary material. Subsequent annealing for 20 min (orange) in dry, low p_{O2} nitrogen at 950 °C showed partial recovery of properties for $p_{H2O} > 10^{-6}$ bar. For $p_{H2O} < 10^{-6}$ bar (<1 ppm), however, the additional 20-min dry anneal resulted in "over-annealing" (discussed below) and a slight increase in R_s. These data show that the impact of annealing in a wet ambient is largely recoverable, but for high implant activation p_{H2O} must be held to $<10^{-8}$ bar. Reducing p_{H2O} in the system to this level requires an extended gas purge before annealing, as discussed further in the supplementary material.

Based on the findings of the impact of p_{O2} and p_{H2O}, the annealing behavior with time and temperature was measured under N_2 ($p_{O2} < 10^{-6}$, $p_{H2O} < 10^{-8}$ bar, $P_{total} = 1$ bar) for 5×10^{19} cm^{-3} implants over 2.5–30 min at temperatures from 850 to 1050 °C, using sequential anneals of single samples to minimize sample variation errors. After sample loading, the furnace was purged for 20 min. Following each anneal, indium contacts were soldered to the corners of the samples, Hall measurements were obtained, and the indium contacts were stripped with HCl; the sample was then loaded for the next anneal step. It is important to note that the "total anneal time" does not correct for the finite time required to reach the set temperature after transfer into the furnace (approximately 2 min). However, the staged annealing does provide monotonic trends with time. Figure 4 shows these staged time annealing results for temperatures from 850 to 1050 °C. At lower temperatures (850–900 °C), there was a strong annealing time dependence to R_s [Fig. 4(a)], which decreased for times up to 30 min as mobility [Fig. 4(b)] and carrier activation [Fig. 4(c)] increased. Even after 30 min, the mobility did not reach the level observed for higher

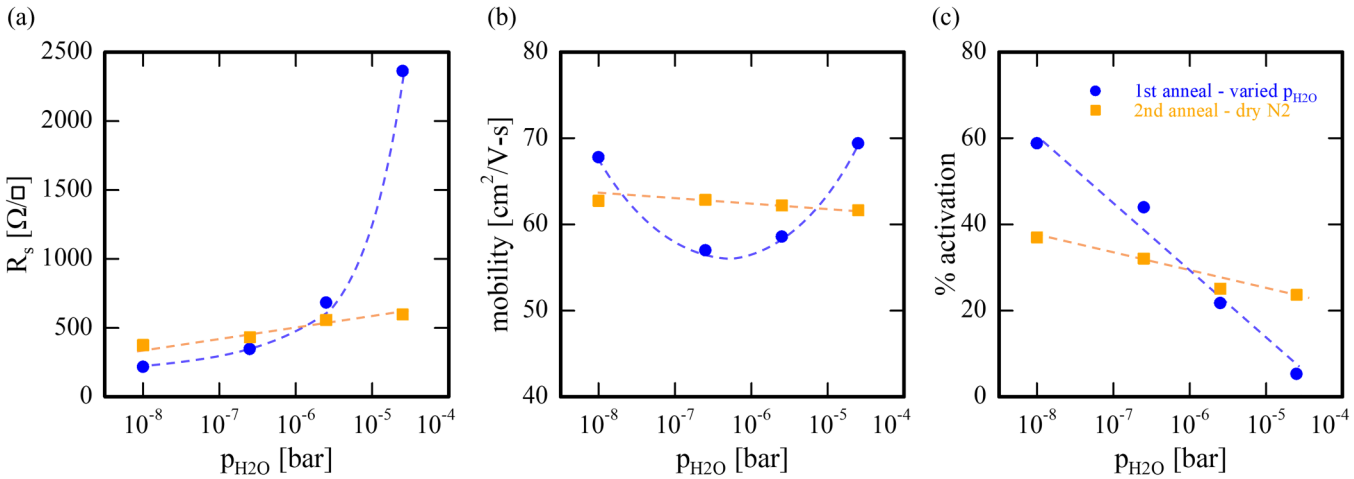

FIG. 3. Plots of R_s (a), μ (b), and % activation (c), as a function of p_{H2O} added to otherwise high purity (R, dried to $p_{H2O} < 10^{-8}$ bar) N_2, showing first anneal (950 °C, 20 min) with varied H_2O content in blue and after a second anneal (950 °C, 20 min) under dry N_2 in orange, showing the recovery of electrical properties. Dashed lines are added as a guide to the eye.

temperature anneals. At higher temperatures (1000 and 1050 °C), the mobility saturated at the shortest anneals, indicating that the implant damage rapidly recovered. However, Si is known to diffuse at temperatures >950 °C[15,24,35] limiting useful annealing to lower temperatures. With extended time at higher temperatures, R_s began to increase associated with a decrease in carrier activation; this "over-annealing" behavior is discussed further below. With these considerations, 950 °C emerges as an optimized annealing temperature with a broad anneal time window of 5–30 min; R_s reached a minimum after only 10 min (corresponding with maximized μ and % activation) and held for 30 min before R_s started to slowly increase.

For long anneal times, the activation fraction decreased resulting in "over-annealing." At 5×10^{19} cm^{-3}, deactivation was observed even at low temperatures, occurring after 40 min at 950 °C but after only 15 min at 1050 °C. Over-annealing in implanted samples manifested as a decrease in active carriers at all anneal temperatures, and with a decrease in mobility at the highest temperatures only. To investigate the dose dependence, samples at 5×10^{18} and 1×10^{20} cm^{-3} were also time-stage annealed with Hall measurements after each step. Figure 5 shows the properties as a function of anneal time (950 °C, $p_{O2} < 10^{-6}$, $p_{H2O} < 10^{-8}$ bar, $P_{total} = 1$ bar). For 5×10^{18} cm^{-3} implants, there was minimal

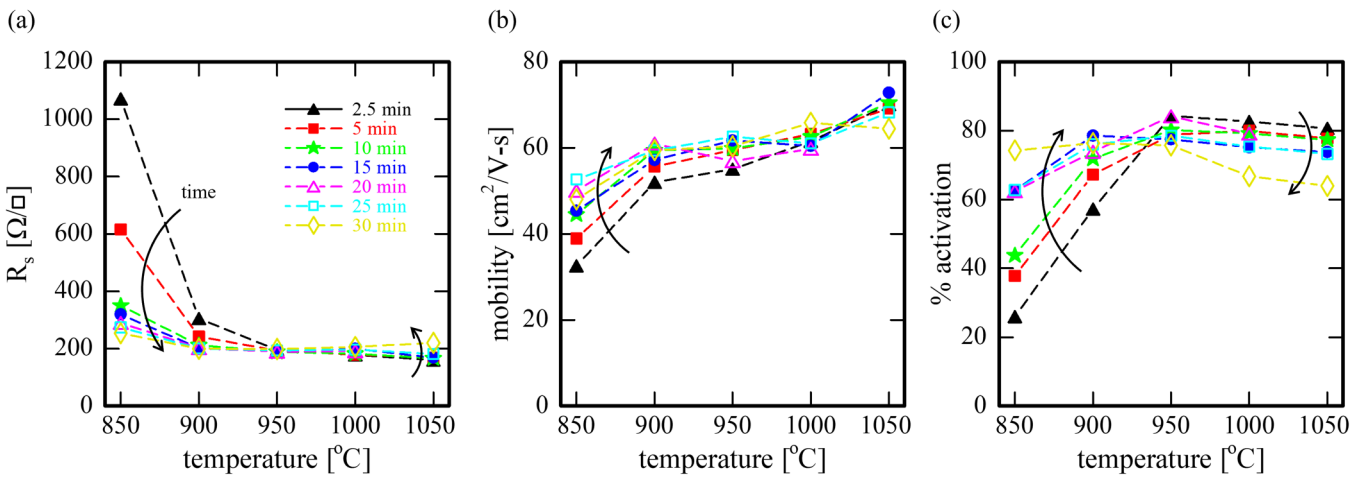

FIG. 4. Plots of R_s (a), μ (b), and % activation (c) vs anneal temperature for different times (indicated by different colors and symbols in the legend), showing trends with time and temperature for anneals under dry N_2. Arrows indicate trends with increasing time, showing a decrease in R_s (a), increase in μ (b), and an increase in carrier activation (c) with time at lower temperatures and a slight increase in R_s (a) with a decrease in carrier activation (c) with time at higher temperatures.

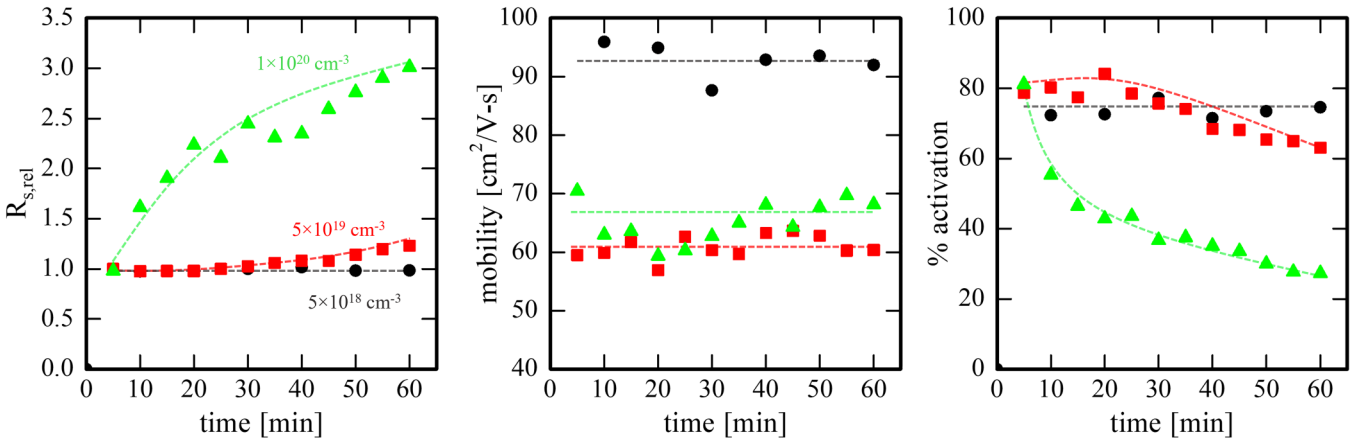

FIG. 5. Plots of $R_{s,rel}$ (=$R_s/R_{s,t=5min}$) (a), μ (b), and % activation (c) vs time for implant conditions 5×10^{18} cm^{-3} (black), 5×10^{19} cm^{-3} (red), and 1×10^{20} cm^{-3} (green) for anneals under dry N_2. No evidence of over-annealing was seen in the 5×10^{18} cm^{-3} sample, minimal over-annealing was observed in the 5×10^{19} cm^{-3} sample after 20 min, and significant over-annealing in the 1×10^{20} cm^{-3} sample occurred after the initial 5 min anneal. Lines are added as a guide to the eye.

change in activation up to 60 min with >70% activation and $\mu > 90$ cm^2/V s. For 5×10^{19} cm^{-3}, anneals for up to 20 min showed 80% activation with $\mu \sim 60$ cm^2/V s, followed by a decrease in carrier activation and a 25% rise in R_s by 60 min. At the highest implant concentration, 1×10^{20} cm^{-3}, there was a very strong time dependence with significant over-annealing even after 10 min. For a 5 min anneal, 81% of the carriers were activated (estimated concentration of 8.14×10^{19} cm^{-3}) with a mobility of 70.8 cm^2/V s and R_s of 75.3 Ω/□. All subsequent anneals reduced the carrier activation and after 60 min R_s increased threefold to 228 Ω/□ with only 28% of the implanted carriers activated. Earlier reports in the literature have suggested that an elevated temperature during implantation is required to activate 1×10^{20} cm^{-3} Si concentration.[17] Our results, however, show that 1×10^{20} cm^{-3} implants can be almost fully activated with high mobility if p_{O2}, p_{H2O}, and time are carefully controlled. As over-annealing is highly correlated to Si concentration, it is likely related to the formation of sub-nm defect pairs,[8] or potentially larger scale (5–10 nm) features arising from the clustering of Si_{Ga} defects as has been seen after annealing at 1100 °C for 30 min in air.[36]

To determine if over-annealing is a result of implant-induced damage, an *in situ* doped 6.9×10^{19} cm^{-3} MOCVD sample was subjected to the same staged anneals at 950 °C. R_s increased from 40 (as grown) to 190 Ω/□ after 30 min with the mobility decreasing from 91 to 58 cm^2/V s and carriers deactivating to 2.3×10^{19} cm^{-3}. These results suggest that the deactivation is not primarily a result of implant damage, but that over-annealing is associated with defects in the film and substrate. Mechanisms may differ between implanted and *in situ* doped samples with the deactivation of the *in situ* doped samples also involving a decrease in mobility, even at 950 °C.

Figure 6 compares deactivation as a function of staged time for samples implanted at 5×10^{19} cm^{-3} from two different epitaxial PAMBE growth runs. Results show that the rate of deactivation is dependent on the sample position within the 23 × 25 mm wafers (likely substrate variations) and is potentially dependent on precise conditions during the epitaxial growth. Samples from the two growths were annealed together to ensure identical thermal

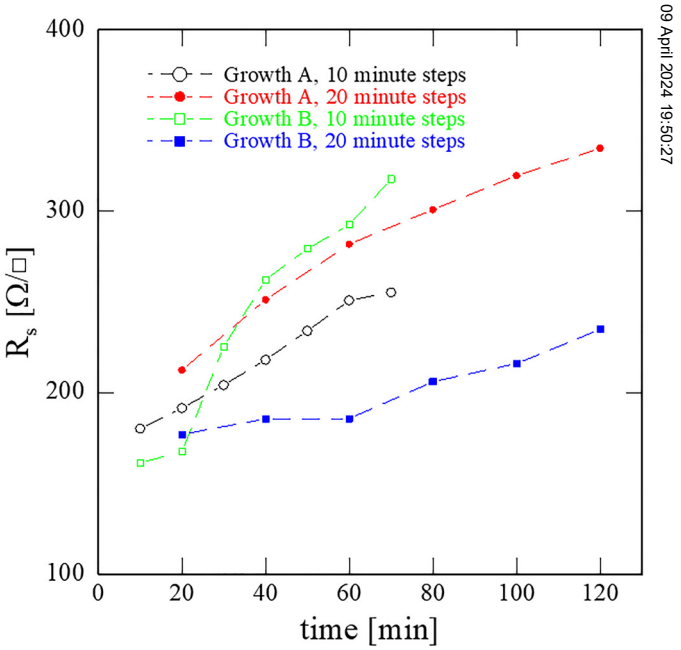

FIG. 6. (a) Plots of R_s vs time for 5×10^{19} cm^{-3} implanted samples from two PAMBE growths (A and B) and two anneal time steps (10 and 20 min) showing that over-annealing began after 20 min (at 950 °C, $p_{O2} < 10^{-6}$, $p_{H2O} < 10^{-8}$ bar, $P_{total} = 1$ bar), but the rate varied depending on specific growth runs and position on the substrate.

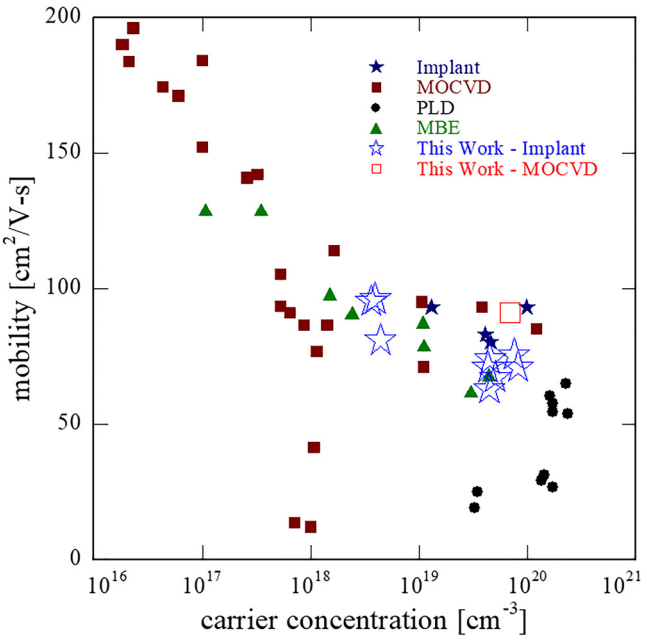

FIG. 7. Blue open stars represent mobility and carrier concentration values for implant samples reported in this study (red open square for *in situ* MOCVD) compared with select literature reports for (010) β-Ga_2O_3 samples doped with Si by implant,[17,19] MOCVD,[10,14,37–39] PLD,[40–42] and MBE.[12,13]

histories, with one pair annealed in 10-min increments and the second pair in 20-min increments. Both pairs show differences in deactivation rates, but the slower deactivating sample in each run came from different epitaxial growth runs. These results indicate that growth-induced defects, which may vary by substrate position and growth method, are likely important in determining the rate of deactivation. The specific defect contributing to this effect is not known but may be related to the density of various defects from growth or doping methods, such as dislocations or extrinsic point defects formed during growth or screw dislocations formed after implant annealing.[24]

The optimized anneal conditions for activating Si in β-Ga_2O_3 vary with implant concentrations, becoming more restrictive as the Si concentration increases. The annealing ambient is critical for activation, requiring $p_{H2O} < 10^{-8}$ bar and $10^{-9} < p_{O2} < 10^{-6}$ bar. Annealing at 950 °C for 5–20 min is sufficient to fully recover the lattice and mobility while minimizing over-annealing, even for concentrations to 1×10^{20} cm^{-3}. Figure 7 compares these Si mobility and carrier activation results from implant and annealing with other literature results for Si in (010) β-Ga_2O_3, as well as the MOCVD *in situ* doped sample results discussed in this paper. For the three implants studied in this work, we observed 94.0 cm^2/V s at 3.95×10^{18} cm^{-3}, 71.6 cm^2/V s at 4.22×10^{19} cm^{-3}, and 70.8 cm^2/V s at 8.15×10^{19} cm^{-3}. These results confirm that implant and thermal anneals are competitive with *in situ* doping methods. The ability to form good ohmic contacts with an average contact resistance $R_c = 0.29 \pm 0.02\ \Omega$ mm was demonstrated by TLM measurements in the 5×10^{19} cm^{-3} samples annealed at 950 °C (see the supplementary material).

B. Implant damage and lattice recovery

To investigate the damage and subsequent recovery, XRD, RBS/c, and STEM were used to analyze samples implanted to 5×10^{19} cm^{-3}. Figure 8(a) shows XRD scans for pre-implant (gray), post-implant (blue), and post-anneal (orange) for 20 min at 950 °C. No additional peaks were seen in the full range 2θ scans after implant or after annealing, though the implanted sample does exhibit shoulders around the (020) peak indicating strain and extended defects within the film; this damage is recovered with annealing. Phase transformations that may have been induced by the implant were not detected by XRD for implant concentrations up to 1×10^{20} cm^{-3} (XRD in Fig. S7 in the supplementary material), likely due to the low total displacements per atom (DPA) for these implant conditions. Additional XRD scans, including rocking curves, and further discussion of the absence of the γ-phase, are included in the supplementary material.

Damage accumulation and recovery was further investigated with RBS/c, as shown in Fig. 8(b) for an as-implanted and annealed (950 °C, 20 min, dry N_2) 5×10^{19} cm^{-3} sample. The random spectrum, with slight planar channeling, matches well with RBS simulations[43,44] of pure Ga_2O_3 (blue). Channeling of the as-implanted sample (red) indicates only partial damage with no fully amorphous layer; the maximum scattering is only 70% of the expected fully amorphous level (scattering expected for a 200 nm Ga_2O_3 film layer is shown in magenta). After annealing, channeling (green) shows full recovery of the crystal lattice with a χ_{min} of 2.8%, consistent with a good single crystal; the de-channeling with depth is also typical for (010) oriented films.[36]

Figure 9 summarizes high-angle annular dark-field (HAADF)-STEM measurements performed on a sample implanted to 5×10^{19} cm^{-3} Si. The image shows defects identified as Ga_i interstitials (blue arrows), regions of retained β-phase (green), and regions of both [110] γ-phase and overlapping γ-phase (pink), as has been repeatedly observed in the literature as implant-induced phase transformations.[22–24] This observed phase transformation supports previous findings that γ-Ga_2O_3 is the kinetically favored structure, often forming in regions of high disorder such as substrate interfaces, free surfaces, and areas with high implant damage.[45] To highlight the implant damage, the Fast Fourier Transform (FFT) of the damaged lattice [Fig. 9(a)] is shown in Fig. 9(b) with the FFT of the annealed, recovered lattice overlaid in green (HAADF-STEM image shown in Fig. S9 in the supplementary material). Overlapping FFT peaks appear white, confirming the presence of the retained β-phase in the damaged lattice; additional diffraction spots present only in the damaged FFT are shown in magenta. Figure 9(c) shows the predicted electron diffraction patterns[46] of both the β-phase along the [010] axis (green) and the γ-phase along the [110] axis (magenta), showing that the overlaid patterns match the FFT of the implanted area, confirming the presence of the γ-phase in the implanted region. Additional images in the supplementary material show a comparable analysis from 90° rotated from the [010] axis.

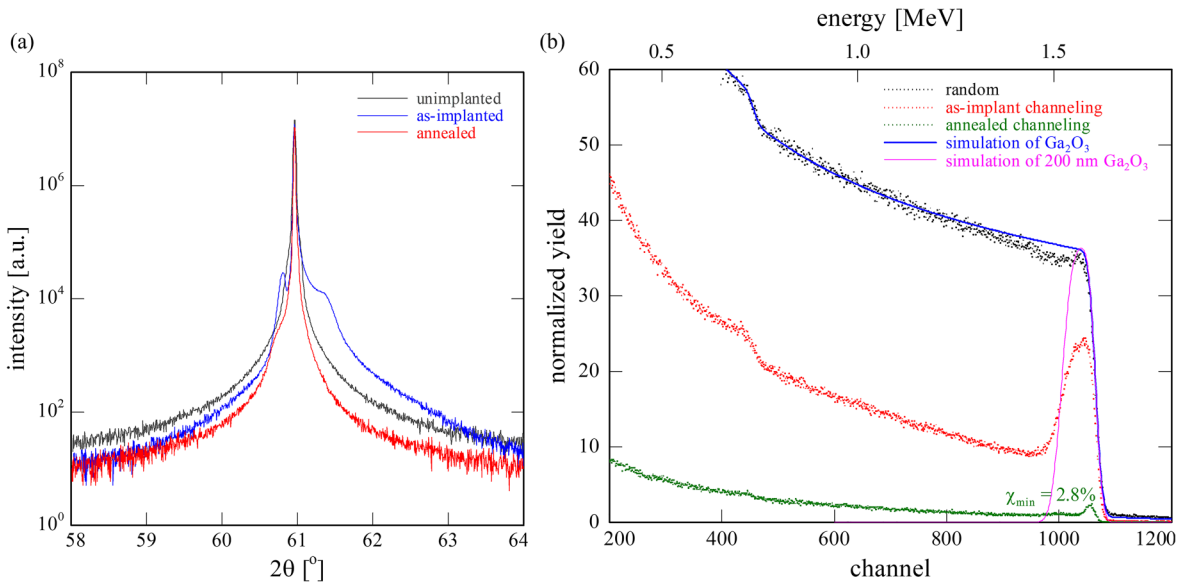

FIG. 8. (a) θ-2θ XRD patterns of (020) reflection for un-implanted (gray), as-implanted to 5×10^{19} cm^{-3} (blue, showing shoulders associated with lattice damage), and implanted and annealed (950 °C, 20 min, N_2, red); and (b) RBS/c spectra compared to simulated spectra showing random (black and blue line, respectively); implanted to 5×10^{19} cm^{-3} channeling in red, showing peak yield in the implanted region not reaching full random signal but matching projected depth of damage (simulated 200 nm in magenta); and after annealing (20 min, 950 °C dry N_2), recovery of the crystal lattice to a near perfect structure shown in green with a χ_{min} of 2.8%.

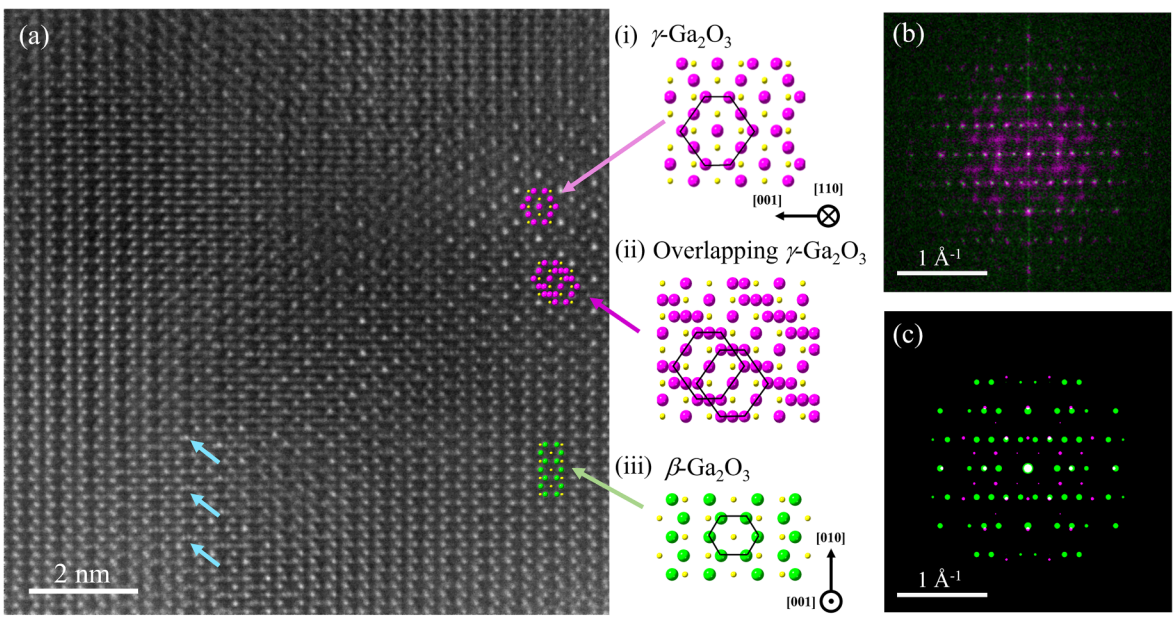

FIG. 9. (a) Atomic resolution HAADF-STEM image of the as-implanted film, highlighting regions of transformed γ-phase (i) and overlapping γ-phase (ii), Ga_i interstitials (blue arrows), and retained β-crystallinity (iii). Green and magenta represent Ga atoms (in β and γ, respectively) and yellow represents O atoms. (b) FFT of the as-implanted region shown in (a) overlaid with the FFT of the β-phase crystal. The magenta shows the additional damage from the implant and white represents areas with intensity from both FFT patterns. Note no pure green spots are observed in the FFT as the implanted region contains both β- and γ-phases. (c) Simulated single crystal electron diffraction patterns along the [010] zone axis of β-Ga_2O_3 and [110] of γ-Ga_2O_3, showing correlation with the measured pattern in (b).

The combined structural information from XRD, RBS/c, and STEM confirms remnant crystallinity in the as-implanted films for the 5×10^{19} cm^{-3} Si implant. It is hypothesized that this remnant crystallinity seeds recovery of the lattice upon annealing, without requiring epitaxial regrowth from below the depth of damage or the substrate.

IV. CONCLUSIONS

With careful control of annealing p_{O2}, p_{H2O}, temperature, and time, Si implant concentrations in β-Ga_2O_3 from 5×10^{18} to 1×10^{20} cm^{-3} can be highly activated (>80%) with full recovery of mobility to >70 cm^2/V s. In the ambient, p_{O2} must be above 10^{-9} bar to maintain stability of Ga_2O_3, with the upper bound being dependent on Si concentration (>1 bar for 5×10^{18} cm^{-3} and 10^{-6} bar for 1×10^{20} cm^{-3}). Water must be minimized during implant annealing with $p_{H2O} < 1 \times 0^{-8}$ bar as even 2.5×10^{-7} bar p_{H2O} reduces active carriers and increases R_s; the impact is even stronger when O_2 is also present in the gas ambient ($p_{O2} > 10^{-6}$ bar). 950 °C is an optimal temperature for activation of all three implant concentrations, maximizing the recovered mobility with minimal diffusion. Anneal time is also critical, especially for high concentrations, with 5 min in a traditional furnace sufficient to activate implants at 950 °C. The upper time limit for annealing is set by the onset of deactivation and depends on Si concentration. At low Si concentrations, deactivation is not observed, after even 60-min anneals, while high Si concentrations begin to deactivate within 10 min. Investigations into the lattice damage and recovery show a high degree of retained β-Ga_2O_3 crystallinity in as-implanted regions, which rapidly seeds lattice recovery and enables annealing at the relatively low temperature of 950 °C. For 5×10^{19} cm^{-3} implants, contact resistances below 0.29 Ω mm can readily be achieved, showing promise for selective area doping methods. Mobility as a function of carrier concentration for implants is comparable to the best reports from *in situ* doped methods, showing that ion implantation is a highly competitive doping method in β-Ga_2O_3.

SUPPLEMENTARY INFORMATION

See the supplementary material for additional implant details, a furnace schematic, a discussion of the importance of purge times, results of annealing Ga_2O_3 in forming gas, contact resistance analysis, additional XRD plots, and additional STEM images.

ACKNOWLEDGMENTS

This research was supported by the Air Force Research Laboratory-Cornell Center for Epitaxial Solutions (ACCESS) under Grant No. FA9550-18-1-0529. The authors also acknowledge use of the Cornell Center for Materials Research Shared Facilities supported through the NSF MRSEC program (No. DMR-1719875) and the Cornell NanoScale Facility, a member of the National Nanotechnology Coordinated Infrastructure (NNCI), which is supported by the National Science Foundation (Grant No. NNCI-2025233).

AUTHOR DECLARATIONS

Conflict of Interest

The authors have no conflicts to disclose.

Author Contributions

Katie R. Gann: Conceptualization (equal); Data curation (lead); Formal analysis (lead); Investigation (equal); Methodology (equal); Validation (lead); Visualization (equal); Writing – original draft (lead); Writing – review & editing (equal). **Naomi Pieczulewski:** Data curation (equal); Formal analysis (supporting); Investigation (equal); Visualization (equal); Writing – review & editing (equal). **Cameron A. Gorsak:** Investigation (equal); Resources (equal); Writing – review & editing (equal). **Karen Heinselman:** Formal analysis (equal); Investigation (equal); Writing – review & editing (equal). **Thaddeus J. Asel:** Investigation (equal); Resources (equal); Writing – review & editing (supporting). **Brenton A. Noesges:** Investigation (equal); Resources (equal); Writing – review & editing (supporting). **Kathleen T. Smith:** Formal analysis (supporting); Investigation (equal); Visualization (supporting); Writing – review & editing (equal). **Daniel M. Dryden:** Investigation (supporting); Writing – review & editing (equal). **Huili Grace Xing:** Supervision (equal); Writing – review & editing (equal). **Hari P. Nair:** Supervision (equal); Writing – review & editing (equal). **David A. Muller:** Supervision (equal); Writing – review & editing (supporting). **Michael O. Thompson:** Conceptualization (equal); Funding acquisition (lead); Project administration (lead); Software (equal); Supervision (lead); Visualization (equal); Writing – review & editing (equal).

DATA AVAILABILITY

The data that support the findings of this study are available from the corresponding author upon reasonable request.

REFERENCES

[1]S. J. Pearton, J. Yang, P. H. Cary, F. Ren, J. Kim, M. J. Tadjer, and M. A. Mastro, Appl. Phys. Rev. **5**, 011301 (2018).
[2]J. A. Spencer, A. L. Mock, A. G. Jacobs, M. Schubert, Y. Zhang, and M. J. Tadjer, Appl. Phys. Rev. **9**, 011315 (2022).
[3]R. Roy, V. G. Hill, and E. F. Osborn, J. Am. Chem. Soc. **74**, 719 (1952).
[4]S. Yoshioka, H. Hayashi, A. Kuwabara, F. Oba, K. Matsunaga, and I. Tanaka, J. Phys.: Condens. Matter **19**, 346211 (2007).
[5]H. Aida, K. Nishiguchi, H. Takeda, N. Aota, K. Sunakawa, and Y. Yaguchi, Jpn. J. Appl. Phys. **47**, 8506 (2008).
[6]Z. Galazka, K. Irmscher, R. Uecker, R. Bertram, M. Pietsch, A. Kwasniewski, M. Naumann, T. Schulz, R. Schewski, D. Klimm, and M. Bickermann, J. Cryst. Growth **404**, 184 (2014).
[7]K. N. Heinselman, D. Haven, A. Zakutayev, and S. B. Reese, Cryst. Growth Des. **22**, 4854 (2022).
[8]S. Lany, APL Mater. **6**, 046103 (2018).
[9]J. B. Varley, A. Perron, V. Lordi, D. Wickramaratne, and J. L. Lyons, Appl. Phys. Lett. **116**, 172104 (2020).
[10]A. Bhattacharyya, C. Peterson, T. Itoh, S. Roy, J. Cooke, S. Rebollo, P. Ranga, B. Sensale-Rodriguez, and S. Krishnamoorthy, APL Mater. **11**, 021110 (2023).
[11]S. H. Jeong, T. Kim, O. Vu, and E. K. Kim, J. Alloys Compd. **877**, 160291 (2021).

[12]J. P. McCandless, V. Protasenko, B. W. Morell, E. Steinbrunner, A. T. Neal, N. Tanen, Y. Cho, T. J. Asel, S. Mou, P. Vogt, H. G. Xing, and D. Jena, Appl. Phys. Lett. **121**, 072108 (2022).
[13]K. Azizie, F. V. E. Hensling, C. A. Gorsak, Y. Kim, N. A. Pieczulewski, D. M. Dryden, M. K. I. Senevirathna, S. Coye, S. L. Shang, J. Steele, P. Vogt, N. A. Parker, Y. A. Birkhölzer, J. P. McCandless, D. Jena, H. G. Xing, Z. K. Liu, M. D. Williams, A. J. Green, K. Chabak, D. A. Muller, A. T. Neal, S. Mou, M. O. Thompson, H. P. Nair, and D. G. Schlom, APL Mater. **11**, 041102 (2023).
[14]L. Meng, Z. Feng, A. F. M. A. U. Bhuiyan, and H. Zhao, Cryst. Growth Des. **22**, 3896 (2022).
[15]K. Sasaki, M. Higashiwaki, A. Kuramata, T. Masui, and S. Yamakoshi, Appl. Phys. Express **6**, 086502 (2013).
[16]M. H. Wong, K. Goto, H. Murakami, Y. Kumagai, and M. Higashiwaki, IEEE Electron Device Lett. **40**, 431 (2019).
[17]A. Sardar, T. Isaacs-Smith, J. Lawson, T. Asel, R. B. Comes, J. N. Merrett, and S. Dhar, Appl. Phys. Lett. **121**, 262101 (2022).
[18]R. H. Horng, A. Sood, F. G. Tarntair, D. S. Wuu, C. L. Hsiao, and S. J. Pratap, Ceram. Int. **48**, 36425 (2022).
[19]J. A. Spencer, M. J. Tadjer, A. G. Jacobs, M. A. Mastro, J. L. Lyons, J. A. Freitas, J. C. Gallagher, Q. T. Thieu, K. Sasaki, A. Kuramata, Y. Zhang, T. J. Anderson, and K. D. Hobart, Appl. Phys. Lett. **121**, 192102 (2022).
[20]M. Higashiwaki, K. Sasaki, T. Kamimura, M. Hoi Wong, D. Krishnamurthy, A. Kuramata, T. Masui, and S. Yamakoshi, Appl. Phys. Lett. **103**, 123511 (2013).
[21]E. A. Anber, D. Foley, A. C. Lang, J. Nathaniel, J. L. Hart, M. J. Tadjer, K. D. Hobart, S. Pearton, and M. L. Taheri, Appl. Phys. Lett. **117**, 152101 (2020).
[22]A. Azarov, C. Bazioti, V. Venkatachalapathy, P. Vajeeston, E. Monakhov, and A. Kuznetsov, Phys. Rev. Lett. **128**, 015704 (2022).
[23]J. García-Fernández, S. B. Kjeldby, P. D. Nguyen, O. B. Karlsen, L. Vines, and Ø Prytz, Appl. Phys. Lett. **121**, 191601 (2022).
[24]H. L. Huang, C. Chae, J. M. Johnson, A. Senckowski, S. Sharma, U. Singisetti, M. H. Wong, and J. Hwang, APL Mater. **11**, 061113 (2023).
[25]M. H. Wong, C. H. Lin, A. Kuramata, S. Yamakoshi, H. Murakami, Y. Kumagai, and M. Higashiwaki, Appl. Phys. Lett. **113**, 102103 (2018).
[26]K. Tetzner, A. Thies, B. T. Eldad, F. Brunner, G. Wagner, and J. Würfl, Appl. Phys. Lett. **113**, 172104 (2018).
[27]M. J. Tadjer, C. Fares, N. A. Mahadik, J. A. Freitas, D. Smith, R. Sharma, M. E. Law, F. Ren, S. J. Pearton, and A. Kuramata, ECS J. Solid State Sci. Technol. **8**, Q3133 (2019).
[28]A. Kuramata, K. Koshi, S. Watanabe, Y. Yamaoka, T. Masui, and S. Yamakoshi, Jpn. J. Appl. Phys. **55**, 1202A2 (2016).
[29]R. Sharma, M. E. Law, C. Fares, M. Tadjer, F. Ren, A. Kuramata, and S. J. Pearton, AIP Adv. **9**, 085111 (2019).
[30]S. Oh, Y. Jung, M. A. Mastro, J. K. Hite, C. R. Eddy, and J. Kim, Opt. Express **23**, 28300 (2015).
[31]S. Ahn, F. Ren, S. Oh, Y. Jung, J. Kim, M. A. Mastro, J. K. Hite, C. R. Eddy, and S. J. Pearton, J. Vac. Sci. Technol. B **34**, 041207 (2016).
[32]R. Togashi, K. Nomura, C. Eguchi, T. Fukizawa, K. Goto, Q. T. Thieu, H. Murakami, Y. Kumagai, A. Kuramata, S. Yamakoshi, B. Monemar, and A. Koukitu, Jpn. J. Appl. Phys. **54**, 041102 (2015).
[33]M. H. Wong, K. Sasaki, A. Kuramata, S. Yamakoshi, and M. Higashiwaki, Appl. Phys. Lett. **106**, 032105 (2015).
[34]J. F. Ziegler, M. D. Ziegler, and J. P. Biersack, Nucl. Instrum. Methods Phys. Res. Sect. B **268**, 1818 (2010).
[35]A. Azarov, V. Venkatachalapathy, L. Vines, E. Monakhov, I. H. Lee, and A. Kuznetsov, Appl. Phys. Lett. **119**, 182103 (2021).
[36]S. B. Kjeldby, A. Azarov, P. D. Nguyen, V. Venkatachalapathy, R. Mikšová, A. MacKová, A. Kuznetsov, O. Prytz, and L. Vines, J. Appl. Phys. **131**, 125701 (2022).
[37]Z. Feng, A. F. M. Anhar Uddin Bhuiyan, M. R. Karim, and H. Zhao, Appl. Phys. Lett. **114**, 250601 (2019).
[38]G. Seryogin, F. Alema, N. Valente, H. Fu, E. Steinbrunner, A. T. Neal, S. Mou, A. Fine, and A. Osinsky, Appl. Phys. Lett. **117**, 262101 (2020).
[39]M. Baldini, M. Albrecht, A. Fiedler, K. Irmscher, R. Schewski, and G. Wagner, ECS J. Solid State Sci. Technol. **6**, Q3040 (2017).
[40]H. M. Jeon, K. D. Leedy, D. C. Look, C. S. Chang, D. A. Muller, S. Badescu, V. Vasilyev, J. L. Brown, A. J. Green, and K. D. Chabak, APL Mater. **9**, 101105 (2021).
[41]K. D. Leedy, K. D. Chabak, V. Vasilyev, D. C. Look, J. J. Boeckl, J. L. Brown, S. E. Tetlak, A. J. Green, N. A. Moser, A. Crespo, D. B. Thomson, R. C. Fitch, J. P. McCandless, and G. H. Jessen, Appl. Phys. Lett. **111**, 012103 (2017).
[42]K. D. Leedy, K. D. Chabak, V. Vasilyev, D. C. Look, K. Mahalingam, J. L. Brown, A. J. Green, C. T. Bowers, A. Crespo, D. B. Thomson, and G. H. Jessen, APL Mater. **6**, 101102 (2018).
[43]M. O. Thompson and L. R. Doolittle, RUMP, v. 4.01, Computer Graphics Service, Windows, 2019 (www.genplot.com).
[44]L. R. Doolittle, Nucl. Instrum. Methods Phys. Res. Sect. B **9**, 344 (1985).
[45]K. R. Gann, C. S. Chang, M. C. Chang, D. R. Sutherland, A. B. Connolly, D. A. Muller, R. B. Van Dover, and M. O. Thompson, Appl. Phys. Lett. **121**, 062102 (2022).
[46]C. S. Chang, N. Tanen, V. Protasenko, T. J. Asel, S. Mou, H. G. Xing, D. Jena, and D. A. Muller, APL Mater. **9**, 051119 (2021).